





## Temperature-dependent properties of the antiferroelectric model $\text{PbZrO}_3$ : An effective Hamiltonian study

Kinnary Patel <sup>1</sup>, Bin Xu <sup>2</sup>, Sergey Prosdandev,<sup>1</sup> Romain Faye,<sup>3</sup> Brahim Dkhil <sup>3</sup>,  
Pierre-Eymeric Janolin <sup>3</sup>, and Laurent Bellaïche<sup>1,\*</sup>

<sup>1</sup>Physics Department and Institute for Nanoscience and Engineering, University of Arkansas, Fayetteville, Arkansas 72701, USA

<sup>2</sup>Institute of Theoretical and Applied Physics, Jiangsu Key Laboratory of Thin Films, School of Physical Science and Technology, Soochow University, Suzhou 215006, China

<sup>3</sup>Université Paris-Saclay, CNRS, CentraleSupélec, Laboratoire SPMS, 91190 Gif-sur-Yvette, France



(Received 26 August 2022; revised 27 October 2022; accepted 29 November 2022; published 19 December 2022)

A novel atomistic effective Hamiltonian scheme, incorporating an original and simple bilinear energetic coupling, is developed and used to investigate the temperature-dependent physical properties of the prototype antiferroelectric  $\text{PbZrO}_3$  (PZO) system. This scheme reproduces very well the known experimental hallmarks of the complex  $Pbam$  orthorhombic phase at low temperatures and the cubic paraelectric state of  $Pm\bar{3}m$  symmetry at high temperatures. Unexpectedly, it further predicts a novel intermediate state also of  $Pbam$  symmetry, but in which antiphase oxygen octahedral tiltings have vanished with respect to the  $Pbam$  ground state. Interestingly, such a new state exhibits a large dielectric response and thermal expansion that remarkably agrees with previous experimental observations and the x-ray experiments we performed. We also conducted direct first-principles calculations at 0 K, which further support such a low-energy phase. Within this fresh framework, a reexamination of the properties of PZO is thus called for.

DOI: [10.1103/PhysRevB.106.214108](https://doi.org/10.1103/PhysRevB.106.214108)

### I. INTRODUCTION

Antiferroelectrics (AFE) form an important class of materials that are characterized by antipolar arrangement of dipoles. Because of the various attractive functionalities provided by these materials, there is a growing interest in their use in technological applications, in particular, for energy storage [1–5].  $\text{PbZrO}_3$  (PZO) is the prototypical antiferroelectric (AFE) perovskite, and AFE archetype, and its characteristics have been studied since the 1950s. Recent research activities were aimed to better understand its properties [6–12]; however, despite intensive investigations, PZO is still puzzling regarding several issues, including the origin and complex nature of its ground state and possible existence of intermediate phases before reaching its paraelectric high-temperature state [13,14]. PZO exhibits a cubic perovskite structure of  $Pm\bar{3}m$  symmetry at high temperatures and an antipolar orthorhombic ground state below a critical temperature  $T_c$ , of about 505 K, which has the space group  $Pbam$  [15,16]. This  $Pbam$  ground state [6–10,12] consists of three structural distortions in terms of phonon mode instabilities of the cubic parent phase. The first one is a strong  $R_4^+$  soft phonon mode associated with the zone boundary  $\frac{2\pi}{a}(\frac{1}{2}, \frac{1}{2}, \frac{1}{2})$   $k$ -point of the cubic first Brillouin zone, where  $a$  is the lattice constant of the five-atom cubic perovskite cell. This mode characterizes an antiphase tilting of the oxygen octahedra about the [110] direction in the perovskite lattice. A second mode is the  $\Sigma_2$  mode and is indexed by the  $\frac{2\pi}{a}(\frac{1}{4}, \frac{1}{4}, 0)$   $k$ -point. The  $\Sigma_2$  mode

consists of complex antipolar displacements of Pb ions along [110] accompanied by some oxygen displacements resulting in an unusual tilting pattern about the [001] pseudocubic axis. There is also a third mode contributing to the  $Pbam$  ground state, but that is rather weak. It has the  $S_4$  symmetry and is associated with the  $\frac{2\pi}{a}(\frac{1}{4}, \frac{1}{4}, \frac{1}{2})$   $k$ -point [17]. It was first assumed that a trilinear coupling between these three modes, i.e.,  $R_4^+$ ,  $\Sigma_2$ , and  $S_4$  modes, plays an important role to stabilize PZO's  $Pbam$  ground state (see, e.g., Refs. [7,8]). However, first-principles studies of Ref. [6] revealed that the contribution of this trilinear term to the total energy is small compared to the energy gain of the ground state with respect to the cubic phase [6]. Recently, a theoretical framework has rather suggested that another trilinear coupling term, which is similar to flexoelectricity but that involves gradients of the octahedral tilt modes rather than strain, is responsible for the ground state of PZO with  $Pbam$  symmetry [18]. In contrast, a recent experimental work using resonant ultrasound spectroscopy has rather suggested biquadratic and higher-order terms couplings through strains between the  $R$  and  $\Sigma$  modes [19]. Remarkably, the authors of Ref. [20] discovered a novel and simpler atomistic energy which only *bilinearly* couples the A-cation displacements and oxygen octahedral tilting [also known as antiferrodistortive distortion (AFD)] in  $\text{ABO}_3$  perovskites and which straightforwardly provided an unified description of many antiferroelectric and incommensurate perovskites, as well as ferrielectrics [21]. This finding, therefore, raises the question if such previously overlooked and simple bilinear coupling is, in fact, the main contributor to stabilize the  $Pbam$  ground state of PZO.

\*Corresponding author: laurent@uark.edu

Moreover, new low-energy phases were recently predicted by first-principles calculations in PZO, such as those of  $Ima2$  and  $Pnam$  symmetries containing 30 atoms and 80 atoms per primitive cell, respectively [7,22,23]. The energy difference between these phases is very small and dramatically depends on the pseudopotentials and other computational details, further emphasizing that PZO is rather challenging to understand and to correctly simulate. PZO has another unsettled related question regarding a possible intermediate phase for temperatures in-between the cubic paraelectric  $Pm\bar{3}m$  state and the antiferroelectric orthorhombic  $Pbam$  ground state. Experimentally, such an intermediate phase is sometimes stabilized for a narrow temperature range between the AFE and the cubic phase but still, the structure of the intermediate phase is not really fully known [24–30]. Depending on the crystal growth conditions, intrinsic or intentional chemical doping/defects may extend the temperature range in which the intermediate phase develops and/or causes the appearance of a second intermediate phase showing isothermal, i.e., time-dependent, transition process [13,31]. A recent first-principles study by Xu *et al.* suggested possible candidates for intermediate phases of PZO [32], including one consisting of a dynamical average between the rhombohedral ferroelectric  $R3c$  phase and antiferroelectric  $Pbam$  phases. Involvement of ferroelectric rhombohedral phases and/or intermediate state was also indicated (1) in a high temperature x-ray diffraction study proposing the existence of a ferroelectric rhombohedral phase on heating the PZO crystal [26] and (2) by Tangantsev *et al.* [10] who studied the lattice dynamics of PZO from x-ray and Brillouin scattering and showed that PZO exhibits an intermediate phase on heating the crystal. One can also find in the literature other possibilities for that intermediate phase, such as one associated with lattice distortion corresponding to the  $M$ -point [ $k = \frac{2\pi}{a}(\frac{1}{2}, \frac{1}{2}, 0)$ ] of the first Brillouin zone — as similar to the phase obtained by the authors of Ref. [16]. Note also that based on several experimental techniques, some polar clusters were proposed to coexist in the paraelectric phase, suggesting that the purely paraelectric state is only achieved above 593 K, i.e., far above  $T_C$  (see Ref. [11]).

The goal of this article is two-fold. First of all, to demonstrate, via the development of a novel *ab initio* effective Hamiltonian ( $H_{\text{eff}}$ ) that the bilinear coupling of Ref. [20] can indeed lead to the stabilization of the complex antiferroelectric orthorhombic  $Pbam$  ground state in PZO. Second, to use such novel atomistic scheme to predict that there is indeed an intermediate state in PZO being in-between the known  $Pm\bar{3}m$  and  $Pbam$  states, but which is a state that has never been previously mentioned in the literature — to the best of our knowledge and that shows instabilities allowing to better understand the reported experimental observations. Effective Hamiltonian calculations yield that such intermediate state can be thought of as originating from the known  $Pbam$  ground state but when removing the  $R_4^+$  phonon mode (and also the  $S_4$  mode). Such a state, which is further confirmed here to be of low energy by conducting additional direct *ab initio* calculations, is coined here in the  $\Sigma$  phase due to the predominance of the  $\Sigma_2$  mode. It also has the  $Pbam$  symmetry, therefore resulting in an isostructural transition in PZO with temperature when going from that phase to the ground state under cooling. Interestingly, the  $H_{\text{eff}}$  computations also provide an

intermediate state that possesses (i) a large dielectric response, as it is experimentally known in PZO for temperatures above the transition towards the ground state [33–41]) and (ii) a thermal expansion that agrees well with our measurements. These calculations also yield pseudocubic lattice parameters that are all close to each other in this intermediate state, which indicates that this novel  $Pbam$   $\Sigma$  state can be thought to be a cubic phase in disguise and thus may explain why it may have been missed up to now. This  $\Sigma$  state is also found to be very close in free energy to a tetragonal ferroelectric  $P4mm$  phase or other ferroelectric states that we believe could be easily triggered through constraints such as chemical doping and defects, as well as the application of external electric or mechanical fields, and, therefore, explain many of the experimental observations.

This article is organized as follows. Section II reports details about theoretical and experimental methods developed and/or used here. Section III provides and discusses the results, while Sec. IV summarizes the article.

## II. METHODS

### A. Effective Hamiltonian

As indicated above, an effective Hamiltonian  $H_{\text{eff}}$  is developed in the aim of understanding and modeling finite-temperature properties of  $\text{PbZrO}_3$  bulk. This  $H_{\text{eff}}$  has the following degrees of freedoms: (1) the local soft modes  $\mathbf{u}_i$  in each five-atom cells  $i$ , which are proportional to the electric dipoles of that cell [42] and that are centered on Pb ions here; (2) the  $\omega_i$  pseudovectors that describes oxygen octahedral tiltings in the unit cells  $i$  [43] and that are centered on Zr ions;  $\omega_i$  is such as its direction is the axis about which the oxygen octahedron of cell  $i$  rotates and its magnitude is the angle (in radians) of such rotation; (3) the  $\{\eta_H\}$  homogeneous strain tensor for which the zero value of its diagonal elements (in Voigt notation)  $\eta_{H,1} = \eta_{H,2} = \eta_{H,3}$  is associated with the calculated first-principles-derived lattice constant of the paraelectric cubic state of  $\text{PbZrO}_3$  at 0 K; and (4)  $\mathbf{v}_i$  vectors that quantify the inhomogeneous strain at each five-atom cell  $i$  [42], and that are centered on Zr ions here.

Following the authors of Refs. [44–46], the total internal energy contains two different main energies

$$E^{\text{tot}} = E^{\text{FE}}(\{\mathbf{u}_i\}, \{\eta_i\}) + E^{\text{tilt}}(\{\omega_i\}, \{\mathbf{u}_i\}, \{\eta_i\}), \quad (1)$$

where  $E^{\text{FE}}$  describes the energetics associated with local modes, elastic variables, and their interactions, while  $E^{\text{tilt}}$  characterizes the energetics involving oxygen octahedral tilts and their couplings with local modes and the total  $\{\eta_i\}$  strain (that is the sum of inhomogeneous and inhomogeneous strains).

As indicated in Ref [42],  $E^{\text{FE}}$  can be decomposed into five terms:

$$E^{\text{FE}} = E^{\text{self}}(\{\mathbf{u}_i\}) + E^{\text{dpl}}(\{\mathbf{u}_i\}) + E^{\text{short}}(\{\mathbf{u}_i\}) + E^{\text{elas}}(\{\eta_i\}) + E^{\text{int}}(\{\mathbf{u}_i\}, \{\eta_i\}), \quad (2)$$

where  $E^{\text{self}}$  is the local mode self-energy,  $E^{\text{dpl}}$  pertains to the long-range dipole-dipole interaction,  $E^{\text{short}}$  represents the short-range interactions between local modes that go beyond dipole-dipole interactions,  $E^{\text{elas}}$  denotes the elastic energy, and

$E^{\text{int}}$  describes the interaction between elastic variables and local modes. As proposed in Ref. [42], these five energies can be written as follows:

$$\begin{aligned}
E^{\text{self}} &= \sum_i \{ \kappa_2 u_i^2 + \alpha u_i^4 + \gamma (u_{ix}^2 u_{iy}^2 + u_{iy}^2 u_{iz}^2 + u_{ix}^2 u_{iz}^2) \}, \\
E^{\text{dpl}} &= \frac{Z^{*2}}{\epsilon_\infty} \sum_{i < j} \frac{\mathbf{u}_i \cdot \mathbf{u}_j - 3(\hat{\mathbf{R}}_{ij} \cdot \mathbf{u}_i)(\hat{\mathbf{R}}_{ij} \cdot \mathbf{u}_j)}{R_{ij}^3}, \\
E^{\text{short}} &= \sum_{i \neq j} \sum_{\alpha\beta} J_{ij\alpha\beta} u_{i\alpha} u_{j\beta}, \\
E^{\text{elas}} &= \frac{N}{2} B_{11} (\eta_1^2 + \eta_2^2 + \eta_3^2) + N B_{12} (\eta_1 \eta_2 + \eta_2 \eta_3 + \eta_3 \eta_1) \\
&\quad + \frac{N}{2} B_{44} (\eta_4^2 + \eta_5^2 + \eta_6^2), \\
E^{\text{int}} &= \frac{1}{2} \sum_i \sum_{\alpha\beta} B_{\alpha\beta} \eta_l(\mathbf{R}_i) u_\alpha(\mathbf{R}_i) u_\beta(\mathbf{R}_i), \quad (3)
\end{aligned}$$

with  $\mathbf{R}_{ij} = \mathbf{R}_i - \mathbf{R}_j$  for which  $\mathbf{R}_i$  and  $\mathbf{R}_j$  are the lattice vectors locating sites  $i$  and  $j$ , respectively.  $\alpha$  and  $\beta$  denote Cartesian components along the [100], [010], and [001] directions that are chosen to span the  $x$ -,  $y$ -, and  $z$ -axes, respectively. The  $i$  index runs over all the Pb ions. For any given Pb-site  $i$ , the  $j$  index in  $E^{\text{dpl}}$  runs over all the other Pb ions. In contrast, the  $j$  index in  $E^{\text{short}}$  “only” runs over the first, second, and third nearest Pb neighbors of the Pb ion located at the site  $i$ .

Furthermore, the  $J_{ij\alpha\beta}$  coefficients in  $E^{\text{short}}$  can be written in the following way for the different nearest neighbor (NN) interactions:

$$\begin{aligned}
\text{first NN: } J_{ij\alpha\beta} &= (j_1 + (j_2 - j_1) |\hat{\mathbf{R}}_{ij,\alpha}|) \delta_{\alpha\beta}, \\
\text{second NN: } J_{ij\alpha\beta} &= (j_4 + \sqrt{2}(j_3 - j_4) |\hat{\mathbf{R}}_{ij,\alpha}|) \delta_{\alpha\beta} \\
&\quad + 2j_5 \hat{\mathbf{R}}_{ij,\alpha} \cdot \hat{\mathbf{R}}_{ij,\beta} (1 - \delta_{\alpha\beta}), \\
\text{third NN: } J_{ij\alpha\beta} &= j_6 \delta_{\alpha\beta} + 3j_7 \hat{\mathbf{R}}_{ij,\alpha} \cdot \hat{\mathbf{R}}_{ij,\beta} (1 - \delta_{\alpha\beta}), \quad (4)
\end{aligned}$$

where  $\delta$  is the Kronecker symbol and  $\hat{\mathbf{R}}_{ij,\alpha}$  represents the  $\alpha$ -component of  $\mathbf{R}_{ij}/R_{ij}$ . A detailed explanation of the  $j_3$  coefficient is mentioned in Ref. [42]. It represents the strength (and sign) of a specific intersite interaction between second nearest neighbor for the local mode.

Regarding the second main energy of Eq. (1), we generalize that found in Refs. [44–47] by writing

$$\begin{aligned}
E^{\text{tilt}}(\{\omega_i\}, \{u_i\}, \{\eta_l\}) &= \sum_i [ \kappa_A \omega_i^2 + \alpha_A \omega_i^4 + \gamma_A (\omega_{ix}^2 \omega_{iy}^2 + \omega_{iy}^2 \omega_{iz}^2 + \omega_{ix}^2 \omega_{iz}^2) ] \\
&\quad + \sum_{ij} \sum_{\alpha\beta} K_{ij\alpha\beta} \omega_{i\alpha} \omega_{j\beta} \\
&\quad + \sum_i \sum_{\alpha} K' \omega_{i,\alpha}^3 (\omega_{i+\alpha,\alpha} + \omega_{i-\alpha,\alpha}) \\
&\quad + \sum_i \sum_{\alpha\beta} C_{\alpha\beta} \eta_l(i) \omega_{i\alpha} \omega_{i\beta} + \sum_{i,j} \sum_{\alpha,\beta} D_{ij,\alpha\beta} u_{j,\alpha} \omega_{i,\alpha} \omega_{i,\beta} \\
&\quad + \sum_{i,j} \sum_{\alpha\beta\gamma\delta} E_{\alpha\beta\gamma\delta} \omega_{i\alpha} \omega_{j\beta} u_{j\gamma} u_{i\delta} + \sum_{i,j} \sum_{\alpha,\beta} F_{ij,\alpha\beta} \omega_{i,\alpha} u_{j,\beta}, \quad (5)
\end{aligned}$$

where the sums over  $i$  run over all the Zr sites. The first sum of  $E^{\text{tilt}}$  describes the onsite contributions associated with the oxygen octahedral tilts, as proposed in Refs. [47–50]. The second and third terms represent short-range interactions between oxygen octahedral tiltings [47,49] being first-nearest neighbors in the Zr sublattice. Note that  $j$  runs over the six Zr sites that are first-nearest neighbors of the Zr site  $i$  in the second term while  $\omega_{i+\alpha,\alpha}$  in the third term denotes the  $\alpha$ -component of the  $\omega$  pseudovector at the site shifted from the Zr site  $i$  to its nearest Zr neighbor along the  $\alpha$  axis. Note also that the  $K_{ij\alpha\beta}$  parameters of this second energy are written as

$$\text{first NN: } K_{ij\alpha\beta} = (k_1 + (k_2 - k_1) |\hat{\mathbf{R}}_{ij,\alpha}|) \delta_{\alpha\beta}. \quad (6)$$

Here,  $k_2$  characterizes the strength and sign of a specific interaction between first nearest neighbors for the tilting modes (it is the equivalent of  $j_2$  shown in Fig. 1 of Ref. [42] but for the tilting degrees of freedom rather than the local modes). Moreover and following Ref. [49], the fourth term of  $E^{\text{tilt}}$  characterizes the interaction between strain and tiltings. As first proposed in Ref. [47], the fifth term (that depends on the  $D_{ij,\alpha\beta}$  coefficients) represents a trilinear coupling between oxygen octahedral tiltings and local modes. The sixth energy, which involves the  $E_{\alpha\beta\gamma\delta}$  parameters, characterizes biquadratic couplings between such tiltings and modes [49]. Note that the  $j$  index runs over the eight Pb ions that are first nearest neighbors of the Zr-site  $i$  in these fifth and sixth terms. Finally, the seventh term is the novelty here with respect to the energies provided in Refs. [47–50]. It represents a recently discovered energy that couples oxygen octahedral tiltings and local modes in a bilinear fashion [20,51]. It is allowed by symmetry and was proposed to explain the occurrence of complex antiferroelectric, ferroelectric, and even incommensurable phases in some materials [20,21,51]. Note that the sum over  $j$  is about the eight Zr sites that are nearest neighbors of the Pb-sites  $i$ . It is given, in a less compact form than in Eq. (5), by

$$\begin{aligned}
\Delta E &= F_{ii} \sum_i [(u_{i,x} + u_{i,y})(-\omega_{i100,z} + \omega_{i010,z} - \omega_{i101,z} \\
&\quad + \omega_{i011,z}) + (-u_{i,x} + u_{i,y})(-\omega_{i,z} + \omega_{i110,z} - \omega_{i001,z} \\
&\quad + \omega_{i111,z}) + \text{cyclicpermutation}], \quad (7)
\end{aligned}$$

where  $F_{ii}$  is a material-dependent constant that characterizes the strength of this coupling. The sum over  $i$  runs over all the five-atom cells of the perovskite structure, and the  $x$ ,  $y$ , and  $z$  subscripts denote the Cartesian components of the  $\mathbf{u}_i$  vectors and  $\omega_i$  pseudovectors.  $\omega_{ilmn}$ , with  $l$ ,  $m$ , or  $n$  being 0 or 1, characterizes the  $\omega$  pseudovectors located at  $a(\hat{x} + m\hat{y} + n\hat{z})$  from that of site  $i$ , with  $a$  being the five-atom lattice parameter and  $\hat{x}$ ,  $\hat{y}$ , and  $\hat{z}$  being the unit vectors along the  $x$ -,  $y$ -, and  $z$ -axes, respectively. Note that the Zr site  $i$  is located at  $-a(\frac{1}{2}\hat{x} + \frac{1}{2}\hat{y} + \frac{1}{2}\hat{z})$  with respect to the Pb site  $i$ . Figure 1 schematizes the coupling terms inherent to the first line of Eq. (7). This new coupling term is important in some systems having Pb atoms (Ref. [20]), and hence relaxors.

All the parameters of this effective Hamiltonian are provided in Table I. They are determined by conducting first-principles calculations using the local density approximation (LDA) [52] within density functional theory. Cells containing

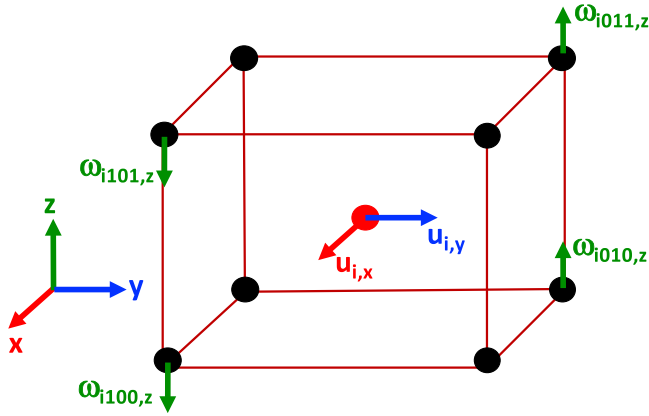


FIG. 1. Sketch of the bilinear coupling terms of the first line of Eq. (7). The red and blue arrows on the central Pb cations represent the  $u_{i,x}$  and  $u_{i,y}$  displacements, respectively. The green arrows on some Zr cations represent the  $\omega$  pseudovectors.

up to 40 atoms are employed, along with the CUSP code [53] and the ultrasoft-pseudopotential scheme [54] with a 25 Ry plane-wave cutoff. Practically, we use the same pseudopotentials than those of Ref. [55], and thus consider the following valence electrons: Pb 5*d*, Pb 6*s*, Pb 6*p*, Zr 4*s*, Zr 4*p*, Zr 4*d*, Zr 5*s*, O 2*s*, and O 2*p* electrons. It is important to know that these effective Hamiltonian parameters are determined by considering small perturbations with respect to the cubic state, and thus do not involve the full ionic and cell relaxation of any phase [42]. Consequently, the fact that we used LDA to obtain these parameters does not automatically imply that our energetic results for *relaxed* structures predicted by the effective Hamiltonian will be closer to those resulting from the direct use of LDA than to those obtained from other functionals such as the generalized gradient approximation (GGA) in the form of revised Perdew-Burke-Ernzerhof [56] (PBEsol). This is especially true if employing these two functionals within first-principles calculations provides similar results in terms of structure, but rather small differences between the total energy of different relaxed phases — as it is, in fact, known in PbZrO<sub>3</sub> bulk [22].

This  $H_{\text{eff}}$ , along with its parameters, is then used in Monte Carlo (MC) computations on  $12 \times 12 \times 12$  supercells (which contains 8640 atoms) for different temperatures. Typically, 40 000 MC sweeps are conducted for each considered temperature, with the first 20 000 sweeps allowing the system to be in thermal equilibrium and the next 20 000 sweeps being employed to obtain statistical averages. However, near phase transitions, a larger number of MC sweeps is needed to have converged results, namely up to 1 million (with the first half used for reaching thermal equilibrium and the next half to extract statistical averages). It is also important to know that a temperature-dependent pressure is added in these Monte Carlo simulations, with this pressure  $P$  acting on the strains to produce the following energy:

$$E_{\text{pres}} = Pa^3(1 + \eta_{H,1})(1 + \eta_{H,2})(1 + \eta_{H,3}), \quad (8)$$

where  $\eta_{H,i}$ , with  $i = 1, 2$ , and  $3$ , being the diagonal elements of the homogeneous strain tensor in Voigt notations [57] (note that the shear strains are neglected in Eq. (8) because they are either null for the cubic paraelectric phase or found to be rather small for the other phases encountered in the simulations). Such a dependence is assumed here to be linear, as proposed in Ref. [58], and is given, in GPa, by:  $P = -5.489655172 - 0.001034483 \times T$ , where  $T$  is the temperature in Kelvin with the two coefficients having been numerically found by trying to reproduce the experimental lattice constants at 10 K and 300 K.

To determine which structural phases are predicted from the effective Hamiltonian simulations, the following quantities are extracted from the outputs of the MC simulations at any investigated temperature

$$u_{\mathbf{k},\alpha} = \frac{1}{N} \sum_i u_{i,\alpha} \exp(i\mathbf{k} \cdot \mathbf{R}_i), \quad (9)$$

$$\omega_{\mathbf{k},\alpha} = \frac{1}{N} \sum_i \omega_{i,\alpha} \exp(i\mathbf{k} \cdot \mathbf{R}_i), \quad (10)$$

where  $\mathbf{k}$  are vectors belonging to the cubic first Brillouin zone,  $\alpha$  denotes Cartesian components, and the sums run over all the five-atom sites. Typically, for the local modes, we look at the  $\mathbf{k}$ -vectors at the zone-center (for the polarization), but also at the  $\Sigma$ -point (for complex antipolar displacements associated with the  $P_{6m}$  state) that is defined as  $\Sigma = (\frac{1}{4}, \frac{1}{4}, 0)$  in  $2\pi/a$

TABLE I. Parameters of the presently developed effective Hamiltonian for PbZrO<sub>3</sub>. Atomic units are used and the reference cubic lattice parameter is 7.763 Bohr.

Dipole	$Z^*$	+6.383	$\epsilon_\infty$	+6.970		
$u$ on-site	$\kappa_2$	+0.00628158	$\alpha$	+0.00943	$\gamma$	-0.00201
$u$ short range	$j_1$	-0.004023	$j_2$	+0.008550		
	$j_3$	+0.000614	$j_4$	-0.0005768	$j_5$	+0.0004896
	$j_6$	+0.0000301	$j_7$	+0.0000151		
Elastic	$B_{11}$	+4.775	$B_{12}$	+1.302	$B_{44}$	+0.0.912
$u$ -strain coup.	$B_{1xx}$	-0.293	$B_{1yy}$	+0.0522	$B_{4yz}$	+0.00294
$\omega$ on-site	$\kappa_A$	-0.15579	$\alpha_A$	+3.523804	$\gamma_A$	-3.20618
$\omega$ short-range	$k_1$	+0.0389464	$k_2$	+0.00413634	$K'$	-0.1241
$\omega$ -strain coup.	$C_{1xx}$	-0.317612	$C_{1yy}$	+1.440823	$C_{4yz}$	-0.011972
$\omega u$ coup. (bilinear)	$F_{ii}$	+0.02117				
$\omega u$ coup. (trilinear)	$D_{ii,xy}$	-0.0430				
$\omega u$ coup. (bi-quadratic)	$E_{xxxx}$	+0.13945	$E_{xyxy}$	+0.339915	$E_{xyyy}$	-0.667303

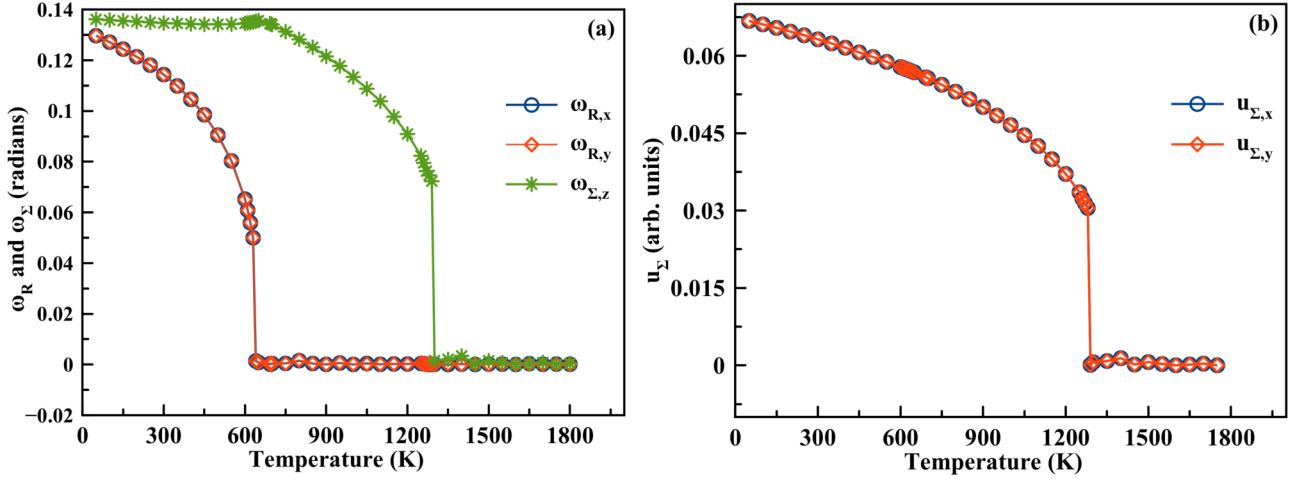


FIG. 2. (a) Temperature dependence of some physical properties of  $\text{PbZrO}_3$  bulk under heating: (a) the  $x$  and  $y$  components of the antiphase tilting ( $\omega_R$ ) and the  $z$ -component of the complex tilting ( $\omega_\Sigma$ ), respectively, of the oxygen octahedra, (b) the  $x$  and  $y$  components of the ( $\mathbf{u}_\Sigma$ ) vector characterizing antipolar displacements centered on Pb cations and associated with the  $\Sigma$  point of the cubic first Brillouin zone.

units. The last point is also investigated for the tilting of the oxygen octahedra, in addition to the  $R$ -point that is given by  $R = (\frac{1}{2}, \frac{1}{2}, \frac{1}{2})$  still in  $2\pi/a$  units. Note that a nonzero  $\omega_{R,\alpha}$  characterizes antiphase tilting about the  $\alpha$ -axis while a finite  $\omega_{\Sigma,\beta}$  should also happen for the  $Pbam$  ground state with  $\beta$  being different from  $\alpha$ .

### B. Direct first-principles calculations

We also used direct first-principles calculations to check some unexpected predictions arising from the use of the effective Hamiltonian and that will be discussed in Sec. III. Practically, we use the generalized gradient approximation (GGA) within the revised Perdew-Burke-Ernzerhof functional (PBEsol) [56], as implemented in the VASP package [59], for these first-principles computations. The projector augmented wave (PAW) [59,60] is also applied to describe the core electrons, and we consider the Pb ( $5d^{10}6s^26p^2$ ), Zr ( $4s^24p^65s^24d^2$ ), and O ( $2s^22p^4$ ) as valence electrons with a 520 eV plane-wave cutoff.

### C. Experiments

The lattice parameters were determined by x-ray diffraction using a high-resolution diffractometer with a Copper radiation ( $\lambda = \text{Cu}_{K\alpha_1} = 1.5405 \text{ \AA}$ ) issued from an 18-kW-rotating anode from room temperature to 750 K using a furnace with a resolution better than 0.1 K. The x-ray diagrams were analyzed fitted with a pseudotetragonal unit cell due to the overlap of the peaks related to the  $a$  and  $b$  lattice parameters of the orthorhombic unit cell. The lattice parameters at 10 K and 300 K were obtained by Rietveld analysis (JANA software) [61] on results obtained from neutron diffraction performed at the Laboratoire Léon Brillouin (beam line 3T2,  $\lambda = 1.2252 \text{ \AA}$ ). The lattice parameters obtained at room temperature from neutron diffraction and from x-ray diffraction are in very good agreement. The orthorhombic unit cell parameters ( $a_o, b_o, c_o$ ) are presented in Fig. 3(b) in a pseudotetragonal ( $a_{pt}, c_{pt}$ ) setting where  $a_o = \sqrt{2}a_{pt}$ ,  $b_o \approx$

$2\sqrt{2}a_{pt}$ , and  $c_o = 2c_{pt}$ . At room temperature the orthorhombic cell parameters are  $a_o = 5.878 \text{ \AA}$ ,  $b_o = 11.783 \text{ \AA}$ ,  $c_o = 8.228 \text{ \AA}$  while, at 10 K, they are  $a_o = 5.878 \text{ \AA}$ ,  $b_o = 11.784 \text{ \AA}$ , and  $c_o = 8.197 \text{ \AA}$ .

## III. RESULTS

### A. Results from the $H_{\text{eff}}$ simulations and x-ray diffractions

Let us now report the predictions of the effective Hamiltonian with the parameters indicated in Table I and the total energy described in Eq. (1), with the additional feature that the second line of Eq. (7) is dropped out. This dropping is made because we numerically found that incorporating all the terms of Eq. (7) provides unphysical solutions for tilting arrangements [such as the tiltings associated with the  $X$ -point of the first Brillouin zone, which is given by  $(0, 0, \frac{1}{2})$  in  $2\pi/a$  units] while keeping the first eight terms of Eq. (7) gives rise to a selected  $Pbam$  ground state [note that dropping all terms of Eq. (7) will not yield the later ground state].

Figure 2(a) reports the temperature evolution of the nonzero tilting-related quantities, namely,  $\omega_{R,x} = \omega_{R,y}$  and  $\omega_{\Sigma,z}$ , while Fig. 2(b) shows that the only significant local mode quantity is  $u_{\Sigma,x} = u_{\Sigma,y}$ , as obtained by heating up the system from the ground state (note that identical results are obtained by cooling down the system and that the  $H_{\text{eff}}$  calculations also provide an  $S_4$  mode, but for which the weight is rather small, namely, less than 0.32%). The fact that all these quantities are finite at small temperature does characterize a  $Pbam$  ground state.

As the temperature increases up to  $\simeq 650 \text{ K}$ ,  $u_{\Sigma,x} = u_{\Sigma,y}$  decreases while  $\omega_{\Sigma,z}$  is barely affected and  $\omega_{R,x} = \omega_{R,y}$  (antiphase oxygen octahedra tilts) gets reduced significantly until vanishing through a jump. A first-order transition to what we call here the  $\Sigma$ -phase, and that is only characterized by nonzero  $u_{\Sigma,x} = u_{\Sigma,y}$  and  $\omega_{\Sigma,z}$  (complex tilts along the  $z$  direction), occurs. The latest phase still has the  $Pbam$  symmetry with space group no. 55 (as indicated by the FINDSYM software [62,63]), therefore indicating that our predicted transition

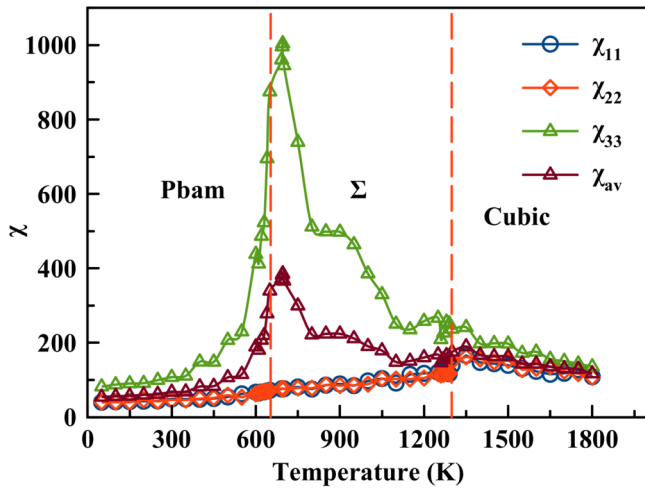


FIG. 3. Temperature dependence of the diagonal elements of dielectric tensor  $\chi_{11}$ ,  $\chi_{22}$ ,  $\chi_{33}$ , and  $\chi_{av}$  [which is  $\frac{1}{3}(\chi_{11} + \chi_{22} + \chi_{33})$ ] of bulk  $\text{PbZrO}_3$ .

around 650 K is isostructural in nature [64–66]. Note that isostructural transitions are usually of first order, which is consistent with the jump of  $\omega_{R,x} = \omega_{R,y}$  seen here at 650 K [7]. Interestingly, it is experimentally known that the *Pbam* ground-state phase disappears around 511 K, which is not so far away from our predicted 650 K — especially taking into account that effective Hamiltonians have the tendency to not accurately predict transition temperatures (while qualitatively reproducing phase transition sequences, as demonstrated, e.g., by Ref. [42]). However, we are not aware of any previous work mentioning that the *Pbam* ground-state phase transforms into another *Pbam* state (that is, the  $\Sigma$  phase here) under heating, therefore making our predictions provocative and novel. Within this  $\Sigma$  phase, Figs. 1(a) and 1(b) indicate that both  $\omega_{\Sigma,z}$  and  $u_{\Sigma,x} = u_{\Sigma,y}$  decrease with temperature and then vanish through a jump at about 1300 K. A first-order transition to cubic paraelectric  $Pm\bar{3}m$  is thus predicted to happen, according to our effective Hamiltonian simulations.

To determine if these rather surprising predictions of the  $H_{\text{eff}}$  can be realistic, Fig. 3 reports the computed  $\chi_{11}$ ,  $\chi_{22}$ , and  $\chi_{33}$  diagonal elements of the dielectric tensor as well as their average  $\chi_{av} = \frac{1}{3}(\chi_{11} + \chi_{22} + \chi_{33})$  as a function of temperature. One can see that  $\chi_{33}$  and thus  $\chi_{av}$  adopt very large values at the temperatures around which the known *Pbam* ground state transforms into the novel  $\Sigma$  phase, which is consistent with the experimental observation of a large dielectric response around the temperatures at which the known *Pbam* ground state disappears [33–41]. Strikingly, the coefficient  $C$  in the fitting of  $\chi_{33}$  and  $\chi_{av}$  by  $\frac{C}{T-T_0}$  is predicted to be  $1.81 \times 10^5$  K and  $1.49 \times 10^5$  K, respectively, in the  $\Sigma$  phase, which is of the same order of magnitude than the experimental values ranging between  $1.36 \times 10^5$  K and  $2.07 \times 10^5$  K (see Refs. [34,67] and references therein) for temperatures at which the known *Pbam* ground state has vanished.

Note that we found that the increase of  $\chi_{av}$  and  $\chi_{33}$  when the temperature gets reduced in the  $\Sigma$  phase towards the known *Pbam* state can be thought to originate from the fact that there is a  $P4mm$  ferroelectric state (with a polarization along the  $z$ -axis and no oxygen octahedral tilting) that is very close in free energy for these temperatures. In fact, reducing the  $F_{ii}$  parameter in Table I to a certain critical value of 0.019 makes the intermediate phase in between the known *Pbam* state and the  $Pm\bar{3}m$  cubic state becoming  $P4mm$  rather than  $\Sigma$ . Note also that the large dielectric response shown in Fig. 3 implies that the zone-center mode should soften when approaching the known *Pbam* phase from above, which has been indeed observed [10,68]. It is also worth mentioning that the proximity in energy of the ferroelectric  $P4mm$  state (or other ferroelectric states) could also explain the experimental electric-field- or defect-driven single ferroelectric  $P$ - $E$  loop observed above the known *Pbam* phase [13], or stabilized under epitaxial strain [69].

Let us now take a look at the behavior of the pseudocubic lattice parameters as a function of temperature. Figure 4(a) reports our predictions from the use of the presently developed effective Hamiltonian (obtained from the strain outputs) while Fig. 4(b) displays our own experimental results along

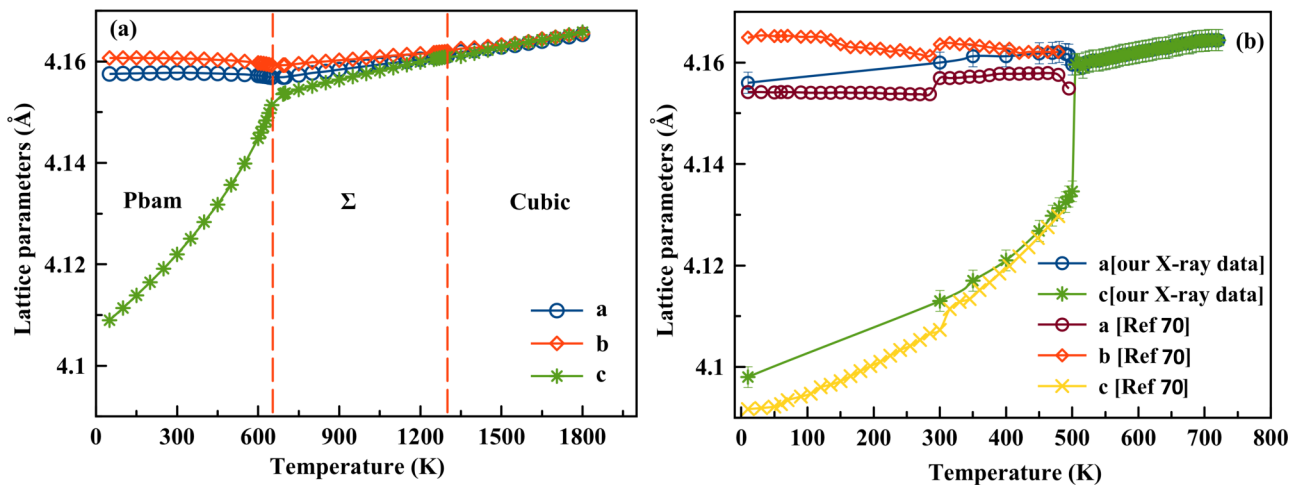


FIG. 4. Temperature dependence of the lattice parameters predicted by the (a) effective Hamiltonian and (b) those measured in the present work as well as in Ref. [70] where a pseudotetragonal unit cell ( $a_{\text{pt}}$ ,  $c_{\text{pt}}$ ) is utilized to represent the orthorhombic phase ( $a_o$ ,  $b_o$ ,  $c_o$ ) where  $a_o = \sqrt{2}a_{\text{pt}}$ ,  $b_o \approx 2\sqrt{2}a_{\text{pt}}$ , and  $c_o = 2c_{\text{pt}}$ .

TABLE II. Energetic gain for different low-energy states with respect to the cubic paraelectric  $Pm\bar{3}m$  state, as predicted by direct first-principles calculations of  $PbZrO_3$ .

Phases	Energy(meV/fu)
$Pbam$	278.8
$R3c$	277.7
$\Sigma$	235.6

with those of Ref. [70]. One can see that, within the known  $Pbam$  state, several features of the measurements are well reproduced, namely, the  $a$  and  $b$  pseudocubic lattice constants are basically independent of the temperature while the  $c$  pseudocubic lattice parameter significantly increases when heating PZO. The jump in the  $c$  lattice constant seen in Fig. 4(a) at around 650 K confirms the first-order character of the isostructural transition between the known  $Pbam$  state and the  $\Sigma$  phase. What is remarkable is that, within the error bars (the range of error bars for the  $a$  and  $b$  pseudocubic lattice parameter is from 0.0013 to 0.007 Å for the whole temperature range, while it is less than 0.0038 Å for the  $c$  lattice parameter), the  $a$ ,  $b$ , and  $c$  parameters are identical within our predicted  $\Sigma$  phase, which may thus give the (wrong) impression that PZO is cubic if solely focusing on pseudocubic lattice pa-

rameters or strains. One can thus think that this  $\Sigma$  phase is a cubic state in disguise, when focusing on pseudocubic lattice parameters. In fact, the predicted temperature evolution of  $\frac{1}{3}(a+b+c)$  adopts a thermal expansion that is very close in the  $\Sigma$  and paraelectric  $Pm\bar{3}m$  phases, and that is characterized by an average coefficient of  $7.97 \times 10^{-6} \text{ K}^{-1}$ , –which is in good agreement with the present measurements giving  $7.4 \times 10^{-6} \text{ K}^{-1}$  (note that such a coefficient is numerically found to be  $7.77 \times 10^{-6} \text{ K}^{-1}$  in our  $\Sigma$  phase versus  $8.36 \times 10^{-6} \text{ K}^{-1}$  in the simulated  $Pm\bar{3}m$  state). This facts suggests, once again, that the present simulations can be realistic. On the other hand, comparing Figs. 4(a) and 4(b) tells us that the jump in the  $c$  pseudocubic lattice parameter when the known  $Pbam$  state disappears is more pronounced in experiments than in our present calculations. Such a quantitative discrepancy can be due to the facts that this disappearance happens at higher temperature in the simulations and/or that the computations use relatively small  $12 \times 12 \times 12$  supercells (implying that the first-order character of that transition can be reduced by the increase in critical temperature and/or finite-size effects).

Interestingly, near the temperatures at which the known  $Pbam$  state disappears, it was observed in Ref. [67] (see Fig. 2.9 there) that the  $(\frac{1}{2}, \frac{3}{2}, \frac{1}{2})$  diffractions peak typically associated with antiphase oxygen octahedral tiltings disappears at a temperature lower than the  $(\frac{1}{4}, \frac{3}{4}, 0)$  diffraction

TABLE III. Crystal structure and atomic positions of the  $Pbam$  and  $\Sigma$  phases at 0 K obtained from first-principles calculations

Pbam phase							
Lattice Constants			Cell angles				
$a$	$b$	$c$	$\alpha$	$\beta$	$\gamma$		
11.782	5.887	8.188	90	90	90		
Fractional coordinates							
Label	Symbol	Multiplicity	Wyckoff label	$x$	$y$	$z$	Occupancy
Pb1	Pb	4	$g$	0.87505	0.20121	0.00000	1
Pb2	Pb	4	$h$	0.87134	0.20890	0.50000	1
Zr1	Zr	8	$i$	0.62378	0.24246	0.24995	1
O1	O	4	$e$	0.00000	0.00000	0.20287	1
O2	O	4	$f$	0.00000	0.50000	0.77054	1
O3	O	8	$i$	0.76195	0.03295	0.28113	1
O4	O	4	$h$	0.09438	0.19920	0.50000	1
O5	O	4	$g$	0.15771	0.22353	0.00000	1
$\Sigma$ phase							
Lattice Constants			Cell angles				
$a$	$b$	$c$	$\alpha$	$\beta$	$\gamma$		
11.717	5.913	4.076	90	90	90		
Fractional coordinates							
Label	Symbol	Multiplicity	Wyckoff label	$x$	$y$	$z$	Occupancy
Pb1	Pb	4	$g$	0.64479	0.30421	0.00000	1
Zr1	Zr	4	$h$	0.61911	0.75709	0.50000	1
O1	O	4	$h$	0.73631	0.45735	0.50000	1
O2	O	2	$d$	0.00000	0.50000	0.50000	1
O3	O	2	$b$	0.00000	0.00000	0.50000	1
O4	O	4	$g$	0.35576	0.28658	0.00000	1

peak that typically characterizes antiparallel displacements of Pb associated with the  $\Sigma$   $k$ -point. Such features appear to be qualitatively consistent with our predictions shown in Figs. 1(a) and 1(b). Note that our predicted  $\Sigma$ -phase can be of short-range or broken into small domains in grown samples, which may explain why it has not been directly reported and reported yet. It is also interesting to realize that, in addition to a zone-center soft-mode, a central mode, with a frequency being very low, was experimentally reported for temperatures above the known *Pbam* state [10,11,68]. Such a feature may be representative of dynamical jumps between different  $\Sigma$ -phases that are with positive or negative  $\omega_{\Sigma,z}$ ,  $\omega_{\Sigma,y}$ , and  $\omega_{\Sigma,x}$ . Such dynamical jumps will render cubic the overall structure of PZO while not affecting  $\frac{1}{3}(a+b+c)$ .

### B. Results from first-principles calculations

Let us now check if such a  $\Sigma$  phase is also seen as a low-energy state within direct first-principles calculations. Table II reports the energy of such  $\Sigma$  phase, but also those of the known *Pbam* and *R3c* states, choosing the zero of energy to correspond to the cubic paraelectric *Pm3m* state. One can first see that the known *Pbam* is the state with the lowest energy, but by only a small amount of about 1 meV/f.u. with respect to *R3c*. Very interestingly, Table II also tells us that  $\Sigma$  is indeed a low-energy state in PZO, with its decrease in energy being about 235.6 meV/f.u. with respect to the cubic state to be compared with 278.8 meV/f.u. for the known *Pbam* phase. In other words, having finite  $\omega_{\Sigma,z}$  and  $u_{\Sigma,x} = u_{\Sigma,y}$  (like in the  $\Sigma$  and known *Pbam* phases) brings about 85% of the energy of the known *Pbam* state with respect to *Pm3m* state, with the other 15% being due to  $\omega_{R,x} = \omega_{R,y}$ . Such percentages highlight the importance of the bilinear couplings of Eq. (7), which are responsible for the finite values of  $\omega_{\Sigma,z}$  and  $u_{\Sigma,x} = u_{\Sigma,y}$  in both the  $\Sigma$  and known *Pbam* states, as well as their low energies. Table III provides the crystal structure and atomic positions of the known *Pbam* and the presently discovered  $\Sigma$  phase, respectively, as predicted by direct first-principles calculations at 0 K, in the hope they can be used in the future to investigate and/or revisit structural phases of PZO. One can see from Table III that the pseudolattice parameters of the  $\Sigma$  phase are not close to each other at 0 K, while they are at high temperatures [see Fig. 4(a).

## IV. CONCLUSION

We developed and used an original atomistic effective Hamiltonian, incorporating the bilinear coupling discovered in Ref. [20] to investigate structural and dielectric properties of bulk PZO as a function of temperature. We also conducted

x-ray diffraction measurements for various temperatures. This effective Hamiltonian reproduces well (i) the existence of the known low-temperature AFE orthorhombic *Pbam* phase and the high-temperature paraelectric cubic phase; (2) the large dielectric response; and (3) the thermal expansion of the pseudocubic lattice parameters of PZO. Its most provocative prediction is the existence of an intermediate phase named here as the  $\Sigma$  phase and that occurs in-between the known *Pbam* and cubic phases. This  $\Sigma$  phase has the *Pbam* symmetry also, therefore yielding an isostructural transition in PZO bulks. It mostly differs from the *Pbam* ground state of PZO by the vanishing of antiphase octahedral tiltings, and its low energy is confirmed by conducting additional direct first-principles calculations. Both the known *Pbam* state and this  $\Sigma$  phase are numerically found to emerge due to the bilinear coupling terms defined in Eq. (7). Possible reasons explaining why this  $\Sigma$  phase may have been previously overlooked are provided here as well. They include the possibilities that the  $\Sigma$  phase only exists in a short-range fashion or is broken into small domains in real materials. Another plausible reason is that its three pseudocubic lattice parameters are basically equal to each other, therefore giving the wrong impression that it is cubic in nature when conducting, e.g., diffractions studies. Moreover, it is also possible that the ferroelectric tetragonal-like phase (that is found to be very close in energy to the  $\Sigma$  phase) is experimentally observed, as it might be triggered under external stimulus (electric field, doping/defects, or stress) which can thus explain some reported polar intermediate phase or polar clusters far above the known *Pbam* state. We hope that the present work, predicting a phase that has never been mentioned in the rich literature of the textbook antiferroelectric compound to the best of our knowledge, will generate new experimental, theoretical, and computational studies and/or analysis on PZO.

### ACKNOWLEDGMENTS

The authors in Arkansas thank the Vannevar Bush Faculty Fellowship (VBFF) Grant No. N00014-20-1-2834 from the Department of Defense and the Office of Naval Research Grant No. N00014-21-1-2086. B.X. thanks the Natural Science Foundation of Jiangsu Province (Grant No. BK20201404), the startup fund from Soochow University and the support from Priority Academic Program Development (PAPD) of Jiangsu Higher Education Institutions. We are also thankful for the computational support from the Arkansas High Performance Computing Center (AHPCC). PEJ and RF thank Dr. F. Porcher from Laboratoire Léon Brillouin for performing the neutron diffraction and Rietveld analyses.

- 
- [1] X. Hao, *J. Adv. Dielect.* **03**, 1330001 (2013).  
 [2] B. Ma, D.-K. Kwon, M. Narayanan, and U. Balachandran, *J. Mater. Res.* **24**, 2993 (2009).  
 [3] B. Ma, M. Narayanan, and U. Balachandran, *Mater. Lett.* **63**, 1353 (2009).

- [4] X. Hao, Y. Wang, L. Zhang, and S. An, *Appl. Phys. Lett.* **102**, 163903 (2013).  
 [5] B. Peng, Q. Zhang, X. Li, T. Sun, H. Fan, S. Ke, M. Ye, Y. Wang, W. Lu, H. Niu, J. F. Scott, X. Zeng, and H. Huang, *Adv. Electron. Mater.* **1**, 1500052 (2015).



- [6] J. Íñiguez, M. Stengel, S. Prosandeev, and L. Bellaiche, *Phys. Rev. B* **90**, 220103(R) (2014).
- [7] S. Prosandeev, C. Xu, R. Faye, W. Duan, H. Liu, B. Dkhil, P.-E. Janolin, J. Íñiguez, and L. Bellaiche, *Phys. Rev. B* **89**, 214111 (2014).
- [8] J. Hlinka, T. Ostapchuk, E. Buixaderas, C. Kadlec, P. Kuzel, I. Gregora, J. Kroupa, M. Savinov, A. Klic, J. Drahoukoupil, I. Etxebarria, and J. Dec, *Phys. Rev. Lett.* **112**, 197601 (2014).
- [9] E. Cockayne and K. M. Rabe, *J. Phys. Chem. Solids* **61**, 305 (2000).
- [10] A. K. Tagantsev, K. Vaideeswaran, S. B. Vakhrushev, A. V. Filimonov, R. G. Burkovsky, A. Shaganov, D. Andronikova, A. I. Rudskoy, A. Q. R. Baron, H. Uchiyama, D. Chernyshov, A. Bosak, Z. Ujma, K. Roleder, A. Majchrowski, J.-H. Ko, and N. Setter, *Nat. Commun.* **4**, 2229 (2013).
- [11] J.-H. Ko, M. Gorny, A. Majchrowski, K. Roleder, and A. Bussmann-Holder, *Phys. Rev. B* **87**, 184110 (2013).
- [12] B. K. Mani, S. Lisenkov, and I. Ponomareva, *Phys. Rev. B* **91**, 134112 (2015).
- [13] H. Liu and B. Dkhil, *Z. Kristallogr.* **226**, 163 (2011).
- [14] X. Tan, C. Ma, J. Frederick, S. Beckman, and K. G. Webber, *J. Am. Ceram. Soc.* **94**, 4091 (2011).
- [15] H. Fujishita, Y. Shiozaki, N. Achiwa, and E. Sawaguchi, *J. Phys. Soc. Jpn.* **51**, 3583 (1982).
- [16] H. Fujishita and S. Hoshino, *J. Phys. Soc. Jpn.* **53**, 226 (1984).
- [17] B. Jaffe, *Proc. IRE* **49**, 1264 (1961).
- [18] K. Shapovalov and M. Stengel, *arXiv:2112.12167*.
- [19] M. A. Carpenter, E. K. H. Salje, M. B. Costab, A. Majchrowski, and K. Roleder, *J. Alloys Compd.* **898**, 162804 (2022).
- [20] K. Patel, S. Prosandeev, Y. Yang, B. Xu, J. Íñiguez, and L. Bellaiche, *Phys. Rev. B* **94**, 054107 (2016).
- [21] T. Ma, Z. Fan, B. Xu, T.-H. Kim, P. Lu, L. Bellaiche, M. J. Kramer, X. Tan, and L. Zhou, *Phys. Rev. Lett.* **123**, 217602 (2019).
- [22] H. Aramberri, C. Cazorla, M. Stengel, and J. Íñiguez, *npj Comput. Mater.* **7**, 196 (2021).
- [23] J. S. Baker, M. Paściak, J. K. Shenton, P. Vales-Castro, B. Xu, J. Hlinka, P. Márton, R. G. Burkovsky, G. Catalan, A. M. Glazer, and D. R. Bowler, *arXiv:2102.08856*.
- [24] E. Sawaguchi, G. Shirane, and Y. Takagi, *J. Phys. Soc. Jpn.* **6**, 333 (1951).
- [25] V. J. Tennery, *J. Electrochem. Soc.* **112**, 1117 (1965).
- [26] V. J. Tennery, *J. Am. Ceram. Soc.* **49**, 483 (1966).
- [27] L. Goulpeau, *Sov. Phys.-Solid State* **8**, 1970 (1967).
- [28] M. Tanaka, R. Saito, and K. Tsuzuki, *Jpn. J. Appl. Phys.* **21**, 291 (1982).
- [29] H. Fujishita, *J. Phys. Soc. Jpn.* **61**, 3606 (1992).
- [30] H. Liu, *J. Am. Ceram. Soc.* **101**, 5281 (2018).
- [31] D. Kajewski, I. J-Sumara, J.-H. Ko, J. W. Lee *et al.*, *Materials* **15**, 4077 (2022).
- [32] B. Xu, O. Hellman, and L. Bellaiche, *Phys. Rev. B* **100**, 020102(R) (2019).
- [33] X. Dai, J.-F. Li, and D. Viehland, *Phys. Rev. B* **51**, 2651 (1995).
- [34] S. Roberts, *J. Am. Ceram. Soc.* **33**, 63 (1950).
- [35] K. Roleder and G. Kugel, *Ferroelectrics* **80**, 161 (1988).
- [36] B. A. Scott and G. Burns, *J. Am. Ceram. Soc.* **55**, 331 (1972).
- [37] G. Shirane, *Phys. Rev.* **84**, 476 (1951).
- [38] Z. Ujma and J. Handerek, *Phys. Status Solidi A* **28**, 489 (1975).
- [39] Z. Ujma and J. Handerek, *Acta Phys. Pol. A* **53**, 665 (1978).
- [40] D. F. Weirauch and V. J. Tennery, *J. Am. Ceram. Soc.* **53**, 229 (1970).
- [41] R. W. Whatmore and A. M. Glazer, *J. Phys. C: Solid State Phys.* **12**, 1505 (1979).
- [42] W. Zhong, D. Vanderbilt, and K. M. Rabe, *Phys. Rev. Lett.* **73**, 1861 (1994); *Phys. Rev. B* **52**, 6301 (1995).
- [43] I. A. Kornev, L. Bellaiche, P. E. Janolin, B. Dkhil, and E. Suard, *Phys. Rev. Lett.* **97**, 157601 (2006).
- [44] L. Chen, B. Xu, Y. Yang, and L. Bellaiche, *Adv. Funct. Mater.* **30**, 1909496 (2020).
- [45] Y. Yang, B. Xu, C. Xu, W. Ren, and L. Bellaiche, *Phys. Rev. B* **97**, 174106 (2018).
- [46] Y. Yang, H. Xiang, and L. Bellaiche, *Phys. Rev. B* **104**, 174102 (2021).
- [47] S. Prosandeev, D. Wang, W. Ren, J. Íñiguez, and L. Bellaiche, *Adv. Funct. Mater.* **23**, 234 (2013).
- [48] D. Albrecht, S. Lisenkov, W. Ren, D. Rahmedov, I. A. Kornev, and L. Bellaiche, *Phys. Rev. B* **81**, 140401(R) (2010).
- [49] I. A. Kornev, S. Lisenkov, R. Haumont, B. Dkhil, and L. Bellaiche, *Phys. Rev. Lett.* **99**, 227602 (2007).
- [50] S. Lisenkov, I. A. Kornev, and L. Bellaiche, *Phys. Rev. B* **79**, 012101 (2009).
- [51] H. J. Zhao, P. Chen, S. Prosandeev, C. Paillard, K. Patel, J. Íñiguez, and L. Bellaiche, *Adv. Electron. Mater.* **8**, 2100639 (2021).
- [52] P. Hohenberg and W. Kohn, *Phys. Rev.* **136**, B864 (1964); W. Kohn and L. J. Sham, *ibid.* **140**, A1133 (1965).
- [53] L. Bellaiche and D. Vanderbilt, *Phys. Rev. B* **61**, 7877 (2000).
- [54] D. Vanderbilt, *Phys. Rev. B* **41**, 7892 (1990).
- [55] R. D. King-Smith and D. Vanderbilt, *Phys. Rev. B* **49**, 5828 (1994).
- [56] J. P. Perdew, A. Ruzsinszky, G. I. Csonka, O. A. Vydrov, G. E. Scuseria, L. A. Constantin, X. Zhou, and K. Burke, *Phys. Rev. Lett.* **100**, 136406 (2008).
- [57] W. Voigt, *Lehrbuch der Kristallphysik* (Teubner, Leipzig, 1910).
- [58] S. Tinte, J. Íñiguez, K. M. Rabe, and D. Vanderbilt, *Phys. Rev. B* **67**, 064106 (2003).
- [59] G. Kresse and D. Joubert, *Phys. Rev. B* **59**, 1758 (1999).
- [60] P. E. Blöchl, *Phys. Rev. B* **50**, 17953 (1994).
- [61] V. Petříček, M. Dušek, and L. Palatinus, *Z. Kristallogr.* **229**, 345 (2014).
- [62] H. T. Stokes, D. M. Hatch, and B. J. Campbell, *FINDSYM, ISOTROPY Software Suite*, [iso.byu.edu](http://iso.byu.edu)
- [63] H. T. Stokes and D. M. Hatch, *J. Appl. Crystallogr.* **38**, 237 (2005).
- [64] V. Ranjan, S. Bin-Omran, L. Bellaiche, and A. Alsaad, *Phys. Rev. B* **71**, 195302 (2005).
- [65] H. Tian, X.-Y. Kuang, A.-J. Mao, Yurong Yang, Changsong Xu, S. O. Seyedaghaee, and L. Bellaiche, *Phys. Rev. B* **97**, 020103(R) (2018).
- [66] B. J. Kennedy, C. J. Howard and B. C. Chakoumakos, *J. Phys.: Condens. Matter* **11**, 1479 (1999).
- [67] Romain Faye thesis: Structures and properties of a model antiferroelectric: PbZrO<sub>3</sub>, <https://tel.archives-ouvertes.fr/tel-01127295> (2014).

- [68] T. Ostapchuk, J. Petzelt, V. Zelezny, S. Kamba, V. Bovtun, V. Porokhonsky, A. Pashkin, P. Kuzel, M. D. Glinchuk, and I. P. Bykov, *J. Phys.: Condens. Matter* **13**, 2677 (2001).
- [69] L. Pintilie, I. Vrejoiu, D. Hesse, G. LeRhun, and M. Alexe, *Phys. Rev. B* **75**, 104103 (2007).
- [70] H. Fujishita, Y. Ishikawa, S. Tanaka, A. Ogawaguchi, and S. Katano, *J. Phys. Soc. Jpn.* **72**, 1426 (2003).